Current Biology 23, 48–52, January 7, 2013 ©2013 Elsevier Ltd All rights reserved http://dx.doi.org/10.1016/j.cub.2012.11.006

Report

Spikes in Mammalian Bipolar Cells Support Temporal Layering of the Inner Retina

Tom Baden,[1,2,*] Philipp Berens,[1] Matthias Bethge,[1,3] and Thomas Euler[1,2]
[1]Werner Reichardt Centre for Integrative Neuroscience (CIN), Bernstein Centre for Computational Neuroscience (BCCN)
[2]Institute for Ophthalmic Research
University of Tübingen, 72076 Tübingen, Germany
[3]Max Planck Institute for Biological Cybernetics, 72076 Tübingen, Germany

Summary

In the mammalian retina, 10–12 different cone bipolar cell (BC) types decompose the photoreceptor signal into parallel channels [1–8], providing the basis for the functional diversity of retinal ganglion cells (RGCs) [9]. BCs differing in their temporal properties appear to project to different strata of the retina's inner synaptic layer [10, 11], based on somatic recordings of BCs [1, 2, 4, 12–14] and excitatory synaptic currents measured in RGCs [10]. However, postsynaptic currents in RGCs are influenced by dendritic morphology [15, 16] and receptor types [17], and the BC signal can be transformed at the axon terminals both through interactions with amacrine cells [18, 19] and through the generation of all-or-nothing spikes [20–24]. Therefore, the temporal properties of the BC output have not been analyzed systematically across different types of mammalian BCs. We recorded calcium signals directly within axon terminals using two-photon imaging [25, 26] and show that BCs can be divided into ≥eight functional clusters. The temporal properties of the BC output were directly reflected in their anatomical organization within the retina's inner synaptic layer: faster cells stratified closer to the border between ON and OFF sublamina. Moreover, ≥three fastest groups generated clear all-or-nothing spikes. Therefore, the systematic projection pattern of BCs provides distinct temporal "building blocks" for the feature extracting circuits of the inner retina.

Results and Discussion

Physiological Classification of Mouse Bipolar Cells and Their Stratification

We recorded from 82 bipolar cells (BCs), 53 of which showed reliable light responses (Experimental Procedures), and reconstructed the morphology of their axon terminal arbors (Figure 1A). Calcium signals of different BC terminals displayed distinctive features in response to a full-field square-wave light stimulus, showing how the stimulus is encoded differentially by different cells (Figure 1B). To sort individual BCs by their light responses into distinct functional types, we used an unsupervised clustering algorithm (Experimental Procedures; see also Figure S1 available online). This allowed clustering of BCs into eight functional types based solely on their physiology (four OFF clusters: $C_{1–4}$; three ON: $C_{6–8}$; one ON-OFF: C_5; Figures 1C and 1D).

The axonal stratification depths within the inner plexiform layer (IPL) of functional groups were highly consistent within each group, with the exception of cluster 8, and corresponded to morphologies of the majority of BC types found in the mouse retina [5] (Figure 2A). For clarity, cluster order was arranged to match mean stratification depth in the IPL. OFF and ON-OFF groups stratified in the OFF sublamina, whereas ON groups stratified in the ON sublamina. Stratifying closest to the inner nuclear layer (lowest depth), C_1 likely reflects type 1 and/or 2 OFF BCs, whereas C_2 probably corresponds to type 4 OFF BCs. $C_{3–5}$ cells likely include type 3a/3b OFF BCs. Stratifying near the border to the OFF sublamina, $C_{6,7}$ presumably correspond to types 5a/5b, 6, and/or 7 ON BCs. Finally, stratification depths of C_8 cells varied considerably throughout the ON sublamina and likely comprised representatives of type 8 and at least one of types 5–7 ON BCs. We could not record calcium changes in the synaptic terminals of type 9 ON BCs [27], because their axonal arbors are sparse and difficult to segregate among heavily labeled rod bipolar cell axon terminals. The latter were labeled but never responded to light, consistent with rods being nearly saturated under our experimental conditions (Experimental Procedures). Taken together, the different functional response clusters comprise the majority of known anatomical types of BCs in the mouse retina and provide for a comprehensive sampling of the excitatory drive forwarded to the inner retina.

Systematic Organization of Response Kinetics across the IPL

Response clusters markedly differed in kinetics, ranging from sustained ($C_{1,8}$) to slowly decaying ($C_{2,3,7}$) and transient ($C_{4–6}$) (Figures 1B and 1C). We quantified rise and decay times (Experimental Procedures) such that, in each case, higher values denote faster calcium responses to steps of light. With the exception of morphologically mixed cluster C_8, both rates of rise (Figure 2B) and decay index (Figure 2C) systematically varied with stratification depth, with the fastest cells occurring nearest the border of the ON and OFF sublamina (40% depth). Therefore, different temporal BC channels systematically stratify at different depths of the IPL, with "transient" cells in the middle and "sustained" cells on either extreme, in striking agreement with excitatory inputs recorded in different types of retinal ganglion cells (RGCs) [10, 28]. In addition, we confirmed the existence of an ON-OFF channel in the OFF sublamina (C_5) [10, 14]. Notably, OFF cells $C_{1,3,4}$ exhibited shorter response delays than all ON and ON-OFF cells (Figure 2D), in agreement with shorter axons and expression of inotropic rather than metabotropic dendritic receptors [17]. However, OFF cells C_2 exhibited a longer response delay compared to all other cells (Figures 2D and 2E).

Spikes in Mouse Bipolar Cells

In response to steps of light, many cells exhibited fast, stochastic calcium events ($_F$events) highly reminiscent of calcium spikes recorded in vivo in fish BCs [22, 23] (Figure 1B). Notably, such $_F$events also occurred sporadically in the absence of systematic light stimulation (e.g., in the ON period of an OFF cell; Figure 1B, asterisk). To assess the propensity of

*Correspondence: thomas.baden@uni-tuebingen.de

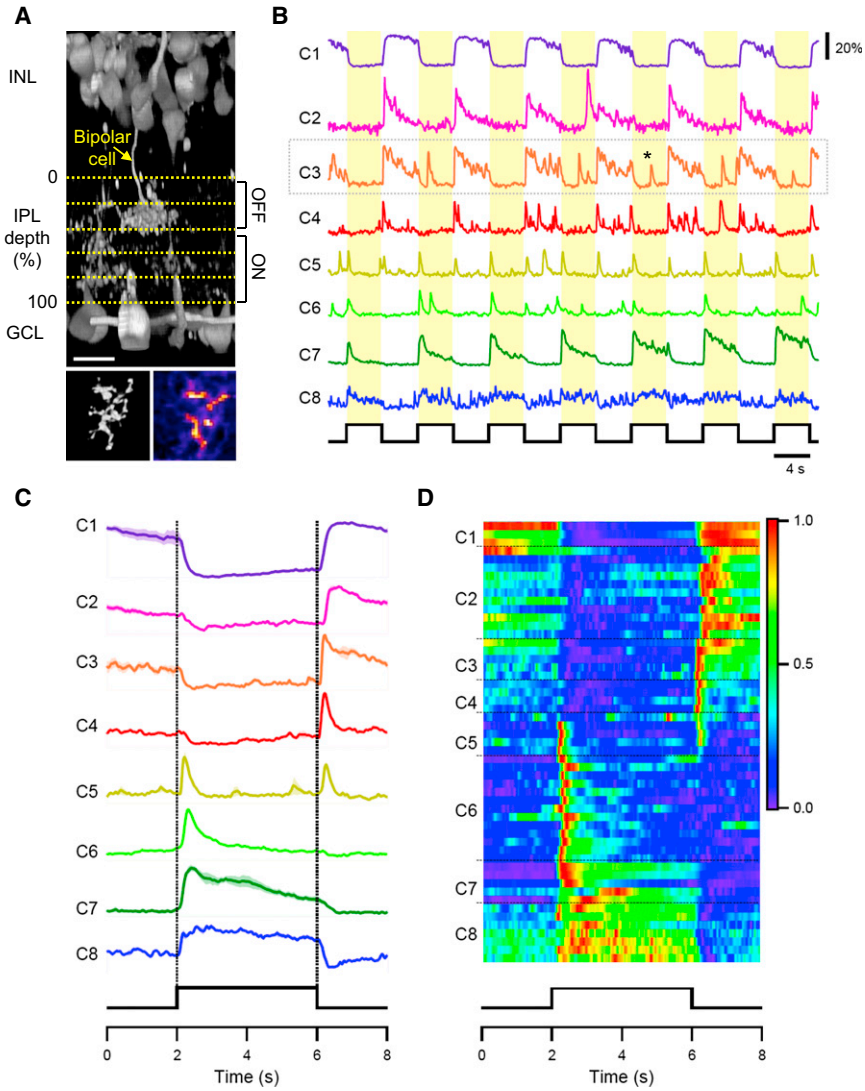

Figure 1. Physiological Classification of Bipolar Cell Light Responses

(A) Morphological reconstruction of a mouse bipolar cell labeled with OGB-1. Top panel shows resliced vertical cross-section; bottom left panel shows a flat-mount view of terminal system; bottom right panel shows the SD of each pixel across the entire image stack of terminal system in response to light stimulation (Experimental Procedures). Scale bar represents 10 μm. INL, inner nuclear layer; IPL, inner plexiform layer; GCL, ganglion cell layer.

(B) Example fluorescence responses (ΔF/F) of different bipolar cell (BC) terminal systems to full-field light stimulation (4 s ON, 4 s OFF), color coded by cluster. The response of the BC shown in (A) is highlighted (dotted box).

(C) Mean responses of eight clusters identified in 53 BC responses to the stimulus used in (B). Error bars represent SD.

(D) Average normalized response of 53 cells sorted into eight clusters (n = 3, 11, 5, 4, 5, 13, 5, and 7 cells in C_{1-8}, respectively).

See also Figure S1.

individual cells to generate $_F$events, we calculated a high-frequency index (HFi), based on the ratio of the power spectral density of each response trace at high frequencies (F_2) and at the stimulus frequency (F_1) (Figures 3A and 3B; Experimental Procedures). Accordingly, a higher HFi denoted response traces dominated by $_F$events, indicative of underlying voltage spikes. Plotting HFi as a function of IPL depth revealed that BCs exhibiting frequent transient $_F$events project nearest the IPL center (Figure 3C). Across C_{1-7} cells, HFi correlated with both rate of rise and decay index (Figures 3D and 3E; Experimental Procedures), consistent with fast voltage spikes generating faster rates of rise and decay of the presynaptic calcium signal compared to slower graded potentials. Across all functional groups, C_{4-6} cells had the highest HFi, rates of rise, and decay index, rendering those cells the most likely candidates to exhibit all-or-nothing voltage spikes driving presynaptic calcium. Two further lines of evidence support this idea. First, waveforms of individual $_F$events were stereotyped (e.g., C_6 cell; Figures 4A and 4B). Both time courses and amplitudes of automatically detected $_F$events (Experimental Procedures) in C_{4-6} cells were highly consistent within each recording (correlation: 0.94 ± 0.02; amplitudes: 0.97 ± 0.11; n = 23 cells), with no significant difference between stimulus-correlated and uncorrelated $_F$events (p > 0.5; n = 23 cells). Moreover, mean $_F$events waveforms recorded in all individual C_{4-6} cells closely resembled each other and were highly reminiscent of an individual voltage spike temporally filtered by the (slower) calcium dynamics that were recorded [29] (Figure 4C). Second, $_F$events in C_4 and C_6 cells exhibited threshold behavior. When stimulated with increasing contrast 100 ms dark/light steps, all $C_{4,6}$ cells displayed highly reproducible all-or-nothing calcium responses over repeated trials (Figure 4D). Moreover, the distribution of normalized response amplitudes to different contrast steps showed a biphasic distribution, with peaks centered around 0 and 1 (Figure 4E). These findings strongly suggest that $_F$events in C_{4-6} cells directly reflect underlying of all-or-nothing voltage spikes in the terminals of BCs.

What of the remaining five response clusters? $C_{3,8}$ cells yielded an intermediate HFi and rates of rise and, like C_{4-6} cells, also exhibited $_F$events (e.g., Figure 1B, traces 3 and 8). However, in these cells, individual $_F$events were more variable in both amplitude and waveform (correlation: 0.87 ± 0.11; amplitudes: 0.83 ± 0.31; n = 11 cells). Here, variability in the shape of $_F$events could result from (1) variable amplitude, graded voltage deflections; (2) inhibitory inputs from amacrine cells [19]; and/or (3) superposition of calcium transients driven by multiple voltage spikes occurring in rapid succession. $C_{1,2,7}$ cells yielded the lowest HFis, rates of rise, and decay index and did not generate clear, isolated $_F$events (e.g., Figure 1B, traces 1, 2, and 7), suggesting that signaling in these cells is dominated by graded potentials. However, even BCs in the most sustained cluster 1 could be interpreted as generating spikes: the increase in variance during the end of the up state in response to the full-field stimulus cannot be explained by an expected increase in shot noise during elevated fluorescence periods. Instead, C1 cells may generate many spikes in

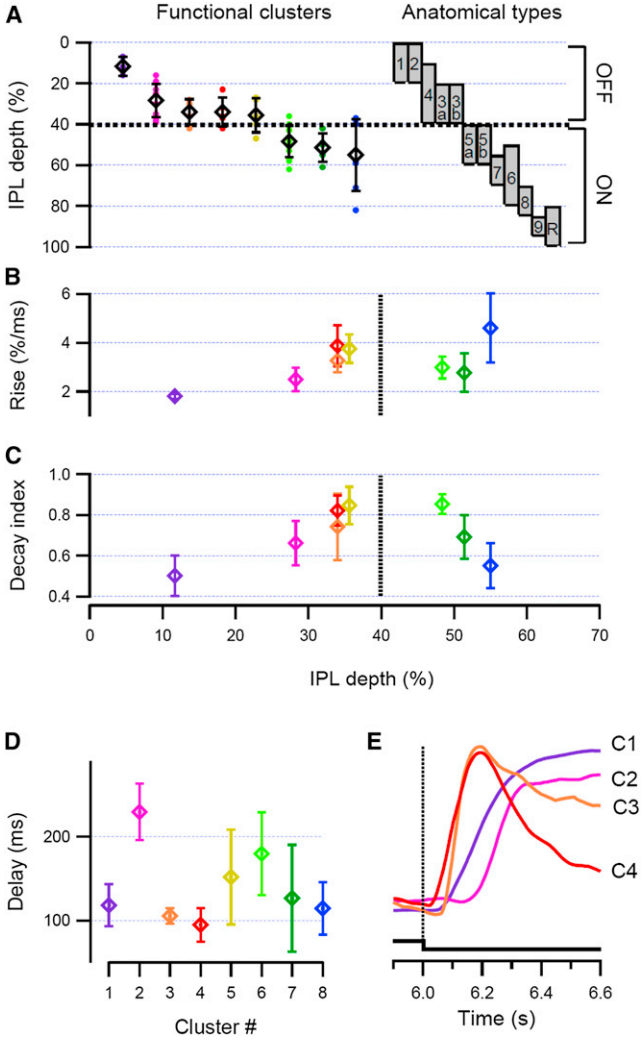

Figure 2. Stratification and Kinetics of BC Clusters

(A) Left: stratification of BC cluster terminal systems in IPL. Right: stratification of known anatomical types [5].

(B and C) Rate of rise (B) and decay index (C) of all clusters as functions of IPL stratification depth.

(D) Mean response delays of individual responses to steps of light. Delays were evaluated at the time when rate of rise was steepest. $C_{1,3,4}$: 106 ± 18 ms; C_2: 234 ± 29 ms; $C_{5,6,7,8}$: 146 ± 54 ms.

(E) Average calcium responses of all OFF clusters to dark step highlights the long response delay of C_2 cells.

Error bars represent SD.

fast succession that cannot be clearly resolved at the level of calcium imaging. By the same argument, kinetically intermediate clusters 2, 3, and 7 could be interpreted as generating spikes riding on top of large graded signals. Clearly, the slow kinetics of calcium transients constrain the assessment of the nature of underlying voltage events, and further studies based on electrical and/or voltage imaging approaches will be required. Another question that needs to be addressed in a future study is whether spikes in mouse BCs are driven by sodium and/or calcium currents. In previous reports, spikes in mammalian BCs (two types in rat [21]; one type in ground squirrel [24]) as well as the largest spikes electrically recorded in fish BCs [23] rely on tetrodotoxin (TTX)-sensitive sodium channels. It is therefore tempting to hypothesize that sodium channels also contribute to the large spikes in presynaptic calcium in mouse $C_{4–6}$ BCs. In support of this notion, bath application of TTX reduces the transience of excitatory inputs to RGCs [30], which may in part be explained by the suppression of sodium spikes in the presynaptic BCs. Spike-like events observed in other mouse BC types may be supported by a combination of Na and calcium channels [23] or exclusively by L-calcium channels [20].

In conclusion, our results demonstrate that the outputs of different mouse BC types form distinct temporal channels, which are systematically organized across the inner plexiform layer [10], consolidating previous findings that the extraction of key temporal features in the visual scene is mainly performed upstream of RGCs [2, 31]. Moreover, light responses of BC terminals near the border of the ON and OFF sublamina generate spikes, which are expected to support a fast and highly transient mode of transmitter release. In contrast, more sustained channels stratify progressively toward each outside border of the IPL and likely favor graded modes of signaling.

Experimental Procedures

Animals and Tissue Preparation

All procedures were performed in accordance with the law on animal protection (Tierschutzgesetz) issued by the German Federal Government and were approved by the institutional animal welfare committee of the University of Tübingen. For all experiments, we used 3- to 6-week-old wild-type mice (C57BL/6J). Animals were housed under a standard 12 hr day/night rhythm. For Ca^{2+} imaging, animals were dark adapted for ≥2 hr. The eyes were quickly enucleated and hemisected in carboxygenated (95% O_2, 5% CO_2) artificial cerebral spinal fluid (ACSF) containing (in mM) 125 NaCl, 2.5 KCl, 2 $CaCl_2$, 1 $MgCl_2$, 1.25 NaH_2PO_4, 26 $NaHCO_3$, 10 glucose, and 0.073 g/l L-glutamine (pH 7.4, 310 mOsmol). The retina was dissected from the eye cup, flattened and mounted onto an Anodisc (13, 0.1 μm pores, Whatman) with ganglion cells facing up, and electroporated with Oregon green BAPTA-1 hexapotassium salt (OGB-1, Invitrogen) as described previously [32]. The tissue was then placed under the microscope, where it was constantly perfused with temperated (~36°C) carboxygenated ACSF with 10 μM sulforhodamine-101 (Invitrogen) added to visualize blood vessels and damaged cells and left to recover for at least 1 hr before recordings were performed.

Two-Photon Ca^{2+} Imaging and Light Stimulation

We used a MOM-type two-photon microscope (designed by W. Denk, Max Planck Institute for Medical Research [MPImF], Heidelberg, Germany; purchased from Sutter Instruments). Both design and procedures were described previously [6, 26]. In brief, the system was equipped with a mode-locked Ti/sapphire laser (MaiTai-HP DeepSee, Newport Spectra-Physics) tuned to ~927 nm, two fluorescence detection channels for OGB-1 (520 BP 30; AHF) and sulforhodamine-101 (622 BP 36; AHF), and a 20× objective (XLUMPlanFL, 0.95 NA, Olympus; or W Plan-Apochromat, 1.0 NA, Zeiss) or 60× objective (CFI APO 60× W NIR Physio, 1.0 NA, Nikon). Image data were acquired with custom software (CfNT by M. Müller, MPImF; or ScanM by M. Müller and T. Euler running under IgorPro 6.2, Wavemetrics), taking 32 × 32 pixel images (15.8 frames per second) for time-lapsed imaging or 512 × 512 pixel stacks (1 μm z steps) for morphological reconstructions. Two different custom-built light stimulators were used. One consisted of a DLP projector (K11, Acer), fitted with band-pass-filtered LEDs (amber, z 578 BP 10; and blue/UV, HC 405 BP 10, AHF/Croma) that roughly match the spectral sensitivity of mouse M and S opsins and were synchronized with the microscope's scanner. The other stimulator employed a modified liquid-crystal-on-silicon i-glasses (EST) illuminated with equivalent filtered LEDs (difference: 400 BP 20 instead of HC 405 BP 10; see [6]). The light from either stimulator was focused through the objective. Stimulator intensity (as photoisomerization rate, $10^3 \cdot P \times s^{-1}$ per cone) was calibrated as described previously [6, 33] to range from 0 (LEDs off) to 13.0 and 12.8 for M and S opsins, respectively. Due to two-photon excitation of photopigments, an additional, steady illumination component of $\sim 10^4 \cdot P \times s^{-1}$ per cone was present during the recordings (for detailed discussion, see [26]). For all experiments, the tissue was kept at a constant mean

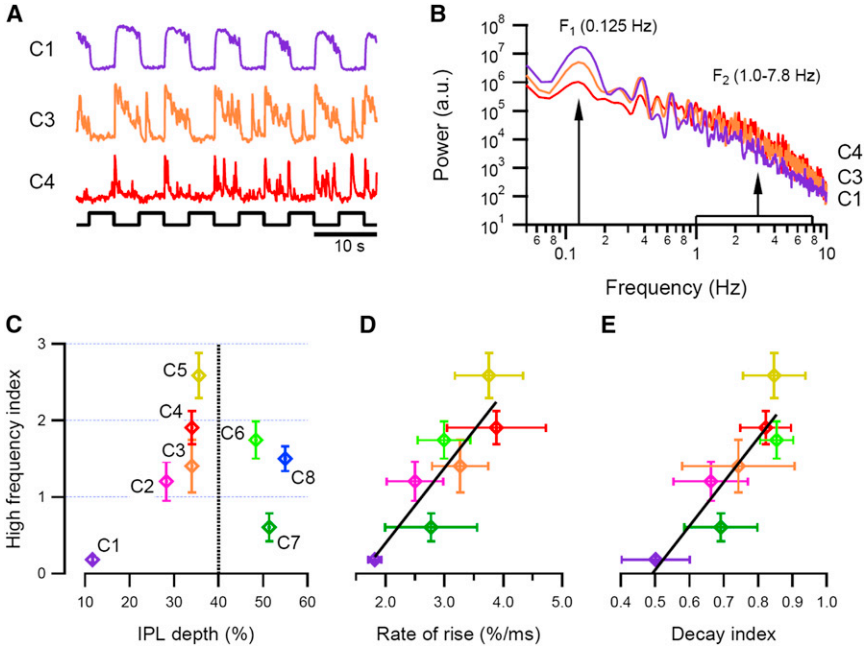

Figure 3. Visual Coding Using Stochastic $_F$Events

(A and B) Calculation of high-frequency index (HFi). We calculated power spectral density (B) from individual BC response traces to the 4 s ON, 4 s OFF stimulus (A). A low power at the stimulus frequency (F_1) and high power and higher frequencies (F_2) yield a higher HFi (Experimental Procedures).

(C) HFi of $C_{1–8}$ cells varied with IPL stratification depth.

(D and E) HFi of $C_{1–7}$ cells scaled linearly with rate of rise and decay index (rise: 0.98 ± 0.25, decay: 5.7 ± 1.3).

Error bars represent SD.

stimulator intensity level for at least 30 s after the laser scanning started before stimuli were presented. Data were analyzed offline using IgorPro (Wavemetrics) and MATLAB (The MathWorks).

Analysis of Imaging Data

Regions of interest of individual BC terminal fields were automatically placed based on thresholding SD of each pixel across the entire image stack of terminal system to light stimulation (e.g., see Figure 1A, bottom right), extracted over time as ΔF/F and aligned with the stimulus, which was recorded in parallel with image acquisition to a precision of 2 ms. The 4 s ON, 4 s OFF full-field stimulus was presented two to nine times per neuron (6.1 ± 1.4 repetitions). Of 82 BCs recorded, we only included data from 53 that passed a response quality criterion QC = $\sum(\sigma^2/n)/\sigma^2_\mu$, where $\sum(\sigma^2/n)$ is the mean variance of all individual light responses and σ^2_μ is the variance of the mean light response. Transient events in ΔF/F traces were automatically detected by application of a threshold criterion of 2.5 times the SD of time-derivative response traces, as described previously [22]. This method reliably identified all fast calcium events ($_F$events) in ΔF/F traces (e.g., Figure 4A). Rate of rise was calculated for individual light responses as the peak time derivative of normalized response traces following a dark-light transition (light-dark transition for OFF and ON-OFF cells). Decay index (DI) was calculated as $DI = (B - E)/(B + E)$, where B and E are the mean fluorescence signal (ΔF/F) across 500 ms at the beginning and at the end of the light response (dark response for OFFs and ON-OFFs), respectively. This index was chosen over exponential fits which were unreliable due to frequent stochastic spike events. High-frequency index (HFi) was calculated as $HFi = \log(10^4 \times F_1/F_2)$, where F_1 and F_2 are the power spectral density of the entire recording trace at the stimulus frequency (0.125 Hz) and the mean power between 1 Hz and the recording Nyquist frequency (7.8 Hz), respectively. Accordingly, a higher HFi indicates responses with a higher prevalence of high-frequency components, suggestive of underlying voltage spikes (see also Figures 3C–3E). The scaling factor of 10^4 was implemented to acknowledge the higher power at lower frequencies, such that HFi ranged between 0 and 3 for the presented data.

Automatic Clustering

To divide the bipolar cell responses into functionally distinct types, we first extracted eight features from the responses to individual steps using principal component analysis. Specifically, we used the first five principal components of ΔF/F traces as well as the first three principal components

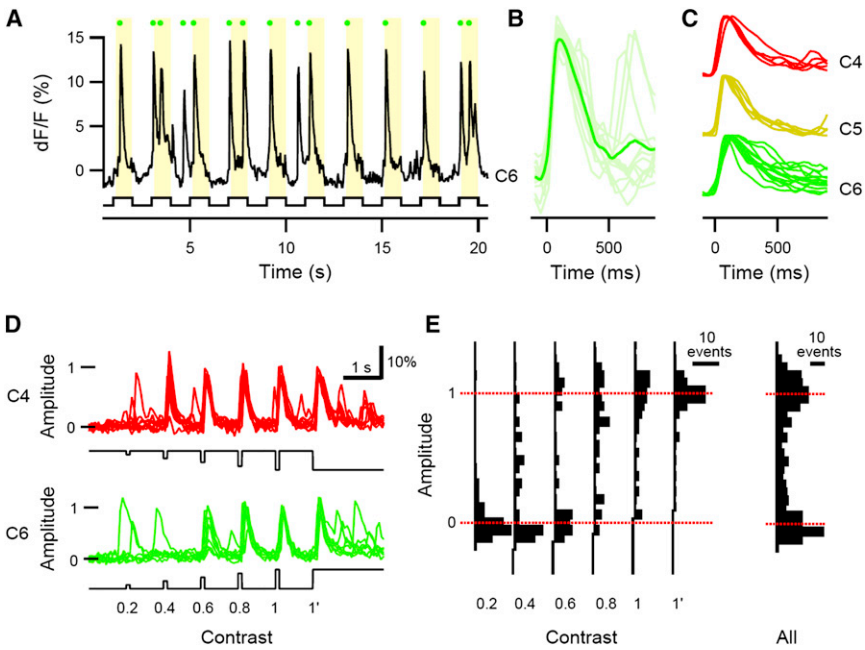

Figure 4. Spikes in Mouse BCs

(A) Response of a C_6 cell to a 0.5 Hz full-field light stimulus, with $_F$events highlighted (Experimental Procedures).

(B) Superposition of $_F$events detected in (A) and average spike waveform.

(C) Superposition of average $_F$events waveform recorded in $C_{4–6}$ cells (n = 5, 5, and 13 cells, respectively).

(D) Top: superposition of 14 responses of a C_4 cell to a series of increasing intensity dark flashes. Bottom: superposition of seven responses of a C_6 cell to increasing contrast light flashes, normalized between baseline (0) and mean $_F$events amplitude (1).

(E) Left: histograms of normalized response amplitudes to increasing contrast light/dark flashes of four C_4 and three C_6 cells. Right: response amplitudes across all contrast levels pooled.

of their temporal derivative (Figure S1A). Next, we fitted the responses to individual steps (n = 322) using a Mixture of Gaussian model [34], as implemented in the Statistics Toolbox of MATLAB. We constrained the covariance matrices to be diagonal. To identify the optimal number of clusters and the optimal regularization parameter, we performed a grid search with candidate cluster numbers C = 1, … ,11 and candidate regularization parameters 10^{-2}, … , 10^{-6}. For each combination of candidate parameters, we evaluated the Bayesian information criterion, $BIC = -2\,logL + M\,logN$, where L is the likelihood of the model, M is the number of parameters, and N is the number of individual responses. The optimal model had seven clusters (Figure S1B), and we assessed the quality of separation by rank-ordering posterior probabilities for each cluster (Figure S1C). To assign a bipolar cell to a functional class, we identified the cluster to which most of repetitions of the cell where assigned. Typically, all repetitions of a cell were assigned the same cluster (Figure S1D). Upon visual inspection (Figure S1E), we found ON cluster 7 to contain at least two different response types, one fully sustained and containing a large degree of high-frequency components, and another slowly decaying with lower power at high frequencies. We therefore divided cells in cluster 7 into clusters 7 and 8, based on a threshold criterion of HFi (see above) (Figure S1E).

Supplemental Information

Supplemental Information includes one figure and can be found with this article online at http://dx.doi.org/10.1016/j.cub.2012.11.006.

Acknowledgments

We thank Timm Schubert for helpful criticisms of the manuscript and Winfried Denk (MPImF, Heidelberg) for supporting the development of the imaging software ScanM. This study was funded by the Deutsche Forschungsgemeinschaft (DFG; EXC307) and is part of the research program of the Bernstein Centre for Computational Neuroscience, Tübingen, funded by the German Federal Ministry of Education and Research (BMBF; FKZ: 01GQ1002).

Received: September 19, 2012
Revised: October 25, 2012
Accepted: November 2, 2012
Published: December 13, 2012

References

1. DeVries, S.H. (2000). Bipolar cells use kainate and AMPA receptors to filter visual information into separate channels. Neuron *28*, 847–856.
2. Awatramani, G.B., and Slaughter, M.M. (2000). Origin of transient and sustained responses in ganglion cells of the retina. J. Neurosci. *20*, 7087–7095.
3. Masland, R.H. (2001). The fundamental plan of the retina. Nat. Neurosci. *4*, 877–886.
4. Wässle, H. (2004). Parallel processing in the mammalian retina. Nat. Rev. Neurosci. *5*, 747–757.
5. Wässle, H., Puller, C., Müller, F., and Haverkamp, S. (2009). Cone contacts, mosaics, and territories of bipolar cells in the mouse retina. J. Neurosci. *29*, 106–117.
6. Breuninger, T., Puller, C., Haverkamp, S., and Euler, T. (2011). Chromatic bipolar cell pathways in the mouse retina. J. Neurosci. *31*, 6504–6517.
7. Light, A.C., Zhu, Y., Shi, J., Saszik, S., Lindstrom, S., Davidson, L., Li, X., Chiodo, V.A., Hauswirth, W.W., Li, W., and DeVries, S.H. (2012). Organizational motifs for ground squirrel cone bipolar cells. J. Comp. Neurol. *520*, 2864–2887.
8. Masland, R.H. (2012). The neuronal organization of the retina. Neuron *76*, 266–280.
9. Gollisch, T., and Meister, M. (2010). Eye smarter than scientists believed: neural computations in circuits of the retina. Neuron *65*, 150–164.
10. Roska, B., and Werblin, F. (2001). Vertical interactions across ten parallel, stacked representations in the mammalian retina. Nature *410*, 583–587.
11. Pang, J.J., Gao, F., and Wu, S.M. (2004). Stratum-by-stratum projection of light response attributes by retinal bipolar cells of Ambystoma. J. Physiol. *558*, 249–262.
12. Wu, S.M., Gao, F., and Maple, B.R. (2000). Functional architecture of synapses in the inner retina: segregation of visual signals by stratification of bipolar cell axon terminals. J. Neurosci. *20*, 4462–4470.
13. DeVries, S.H., Li, W., and Saszik, S. (2006). Parallel processing in two transmitter microenvironments at the cone photoreceptor synapse. Neuron *50*, 735–748.
14. Euler, T., and Masland, R.H. (2000). Light-evoked responses of bipolar cells in a mammalian retina. J. Neurophysiol. *83*, 1817–1829.
15. Poleg-Polsky, A., and Diamond, J.S. (2011). Imperfect space clamp permits electrotonic interactions between inhibitory and excitatory synaptic conductances, distorting voltage clamp recordings. PLoS ONE *6*, e19463.
16. Schachter, M.J., Oesch, N., Smith, R.G., and Taylor, W.R. (2010). Dendritic spikes amplify the synaptic signal to enhance detection of motion in a simulation of the direction-selective ganglion cell. PLoS Comput. Biol. *6*, e1000899.
17. Brandstätter, J.H., Koulen, P., and Wässle, H. (1998). Diversity of glutamate receptors in the mammalian retina. Vision Res. *38*, 1385–1397.
18. Oltedal, L., Mørkve, S.H., Veruki, M.L., and Hartveit, E. (2007). Patch-clamp investigations and compartmental modeling of rod bipolar axon terminals in an in vitro thin-slice preparation of the mammalian retina. J. Neurophysiol. *97*, 1171–1187.
19. Eggers, E.D., and Lukasiewicz, P.D. (2011). Multiple pathways of inhibition shape bipolar cell responses in the retina. Vis. Neurosci. *28*, 95–108.
20. Protti, D.A., Flores-Herr, N., and von Gersdorff, H. (2000). Light evokes Ca2+ spikes in the axon terminal of a retinal bipolar cell. Neuron *25*, 215–227.
21. Cui, J., and Pan, Z.H. (2008). Two types of cone bipolar cells express voltage-gated Na+ channels in the rat retina. Vis. Neurosci. *25*, 635–645.
22. Dreosti, E., Esposti, F., Baden, T., and Lagnado, L. (2011). In vivo evidence that retinal bipolar cells generate spikes modulated by light. Nat. Neurosci. *14*, 951–952.
23. Baden, T., Esposti, F., Nikolaev, A., and Lagnado, L. (2011). Spikes in retinal bipolar cells phase-lock to visual stimuli with millisecond precision. Curr. Biol. *21*, 1859–1869.
24. Saszik, S.D.S., and DeVries, S.H. (2012). A mammalian retinal bipolar cell uses both graded changes in membrane voltage and all-or-nothing Na+ spikes to encode light. J. Neurosci. *32*, 297–307.
25. Denk, W., Strickler, J.H., and Webb, W.W. (1990). Two-photon laser scanning fluorescence microscopy. Science *248*, 73–76.
26. Euler, T., Hausselt, S.E., Margolis, D.J., Breuninger, T., Castell, X., Detwiler, P.B., and Denk, W. (2009). Eyecup scope—optical recordings of light stimulus-evoked fluorescence signals in the retina. Pflugers Arch. *457*, 1393–1414.
27. Haverkamp, S., Wässle, H., Duebel, J., Kuner, T., Augustine, G.J., Feng, G., and Euler, T. (2005). The primordial, blue-cone color system of the mouse retina. J. Neurosci. *25*, 5438–5445.
28. Pang, J.J., Gao, F., and Wu, S.M. (2003). Light-evoked excitatory and inhibitory synaptic inputs to ON and OFF alpha ganglion cells in the mouse retina. J. Neurosci. *23*, 6063–6073.
29. Vogelstein, J.T., Packer, A.M., Machado, T.A., Sippy, T., Babadi, B., Yuste, R., and Paninski, L. (2010). Fast nonnegative deconvolution for spike train inference from population calcium imaging. J. Neurophysiol. *104*, 3691–3704.
30. Ichinose, T., Shields, C.R., and Lukasiewicz, P.D. (2005). Sodium channels in transient retinal bipolar cells enhance visual responses in ganglion cells. J. Neurosci. *25*, 1856–1865.
31. Asari, H., and Meister, M. (2012). Divergence of visual channels in the inner retina. Nat. Neurosci. *15*, 1581–1589.
32. Briggman, K.L., and Euler, T. (2011). Bulk electroporation and population calcium imaging in the adult mammalian retina. J. Neurophysiol. *105*, 2601–2609.
33. Wei, T., Schubert, T., Paquet-Durand, F., Tanimoto, N., Chang, L., Koeppen, K., Ott, T., Griesbeck, O., Seeliger, M.W., Euler, T., and Wissinger, B. (2012). Light-driven calcium signals in mouse cone photoreceptors. J. Neurosci. *32*, 6981–6994.
34. Bishop, C.M. (2007). Pattern Recognition and Machine Learning (Berlin: Springer).